ELSEVIER

Shapes of the saturnian icy satellites and their significance

P.C. Thomas [a,*], J.A. Burns [a], P. Helfenstein [a], S. Squyres [a], J. Veverka [a], C. Porco [b], E.P. Turtle [c],
A. McEwen [d], T. Denk [e], B. Giese [f], T. Roatsch [f], T.V. Johnson [g], R.A. Jacobson [g]

[a] *Center for Radiophysics and Space Research, Cornell University, Ithaca, NY 14853, USA*
[b] *Space Science Institute, 4750 Walnut Street, Boulder, CO 80301, USA*
[c] *Johns Hopkins University Applied Physics Laboratory, 11100 Johns Hopkins Rd., Laurel, MD 20723, USA*
[d] *Department of Planetary Sciences, University of Arizona, Tucson, AZ 85721, USA*
[e] *Institut für Geologische Wissenschaften, Freie Universität, 12249 Berlin, Germany*
[f] *Institute of Planetary Research, German Aerospace Center, Rutherfordstrasse 2, 12489 Berlin, Germany*
[g] *Jet Propulsion Laboratory, California Institute of Technology, 4800 Oak Grove Drive, Pasadena, CA 91109, USA*

Abstract

The sizes and shapes of six icy saturnian satellites have been measured from Cassini Imaging Science Subsystem (ISS) data, employing limb coordinates and stereogrammetric control points. Mimas, Enceladus, Tethys, Dione and Rhea are well described by triaxial ellipsoids; Iapetus is best represented by an oblate spheroid. All satellites appear to have approached relaxed, equilibrium shapes at some point in their evolution, but all support at least 300 m of global-wavelength topography. The shape of Enceladus is most consistent with a homogeneous interior. If Enceladus is differentiated, its shape and apparent relaxation require either lateral inhomogeneities in an icy mantle and/or an irregularly shaped core. Iapetus supports a fossil bulge of over 30 km, and provides a benchmark for impact modification of shapes after global relaxation. Satellites such as Mimas that have smoother limbs than Iapetus, and are expected to have higher impact rates, must have relaxed after the shape of Iapetus was frozen.
© 2007 Elsevier Inc. All rights reserved.

Keywords: Saturn, satellites; Satellites, shapes; Interiors

1. Introduction

Saturn's system of satellites includes seven approximately ellipsoidal objects and dozens of smaller ones with irregular shapes. The larger satellites display a wide range of surface features, albedos, and mean densities. Ellipsoidal objects may be equilibrium shapes determined by their mean density, mass distribution, and spin rates (Chandrasekhar, 1969; Dermott, 1979), and as such their shapes may contain information on their interiors. Likewise, departures from equilibrium forms may reveal information on processes that complicate or defeat tendencies to relax to equilibrium shapes. Cassini data permit measurement of the shapes and masses of most of the ellipsoidal satellites sufficiently well to test models of the interior structure and the extent of relaxation.

In this work we first review the method of shape determination and evaluation. Next we report the measurement results for six satellites (Fig. 1). We then examine how close each moon is to an equilibrium shape. Then we view the results in toto, and finally evaluate the significance of departures from equilibrium forms. We do not consider the largest satellite Titan, as ISS cannot detect the satellite's surface limb and shape measurement requires a global network of control points, which are not yet available.

2. Methods and data

2.1. Shape measurement

The overall shapes are found by measuring limb positions in the ISS images. The process involves these steps: (1) Mea-

---

sure the coordinates of limbs to ~0.1 pixels in the images by techniques described in Thomas et al. (1998). (2) Remove camera distortions and scale limb positions to distance (now given in km) from an approximate center in the image plane. (3) Test if individual limbs are well fit by ellipses. (4) Combine views from different orientations and test for the best-fit ellipsoid and adjust centers in all the images. (5) Examine residuals from the fit ellipsoid to see if an ellipsoid approximation is appropriate. (6) Compare the ellipsoid to equilibrium forms.

The resolution of the images, in pixels/diameter, is sufficiently good that most of a shape's uncertainty derives from the topography, i.e., the deviations from perfect ellipsoidal outlines. Topography on the ellipse can bias centering and thus affect the overall solution. The best images would be 360° limb arc views which highly constrain the center. Views that include transits across Saturn, or include Saturnshine on the dark limb, provide data with more than 180° of arc and greatly reduce the centering uncertainties. In the absence of transits or Saturnshine, low phase angles that provide at least 180° of arc are required. Our techniques also require having the entire limb within one ISS frame (1024 × 1024 pixels). The ellipsoid axes (a, b, c) are found by comparing each image's limb coordinates to the predicted projected ellipse given the ellipsoid shape and camera orientation and viewpoint relative to the object's axes (see (Dermott and Thomas, 1988) for ellipsoidal projections and fitting ellipses). Residuals are the radial differences in pixels between predicted and observed limb positions.

2.2. Evaluation of uncertainties

We use a formal method of uncertainty calculation, checked by other estimates. The accuracy of the limb-finding software can be evaluated by comparing results from images of very different resolution. Enceladus images having better than 2 km/pixel scale and those with 16 km/pixel scale give mean radii differing by 1.3 km. In combination with results from very low-resolution data taken of the Galilean satellites (known sizes), we conclude that uncertainties due to the limb-finding algorithm are ~0.1 pixels. The precision is frequently of order 0.05 pixels. For most fits this uncertainty is small compared to the uncertainty introduced by roughness of the topography. To determine the allowable range of solutions for a, b, c axes, the residuals calculated in pixels were allowed to increase above the minimum by an unrelated 0.1 pixels, equivalent to the measurement uncertainty. The resulting range of allowed solutions depends upon the image resolutions, limb roughnesses, and spacing of the observed limbs around the object. Uncertainties in $(a - c)$ do not equal sums of the uncertainties in a and c because the solutions of the different axes are, to varying degrees, linked in the various data sets. That is, the maximum $(a - c)$ is not necessarily the difference of the maximum a and the minimum c allowed.

We have also used partial data sets to evaluate the uncertainties of not employing all of the limb; these errors can cause fit centers to vary, hence affect the fit axes. For Mimas, removing about 10% of the data points from the ends of profiles changed all three fit axes by 0.1 km. For Enceladus the data were also split into those with pixel scales greater than 2 km and those less than 2 km. Solutions with each set were within 0.2 km for all axes, and mean radii varied by only 0.1 km. We conclude that the formal errors listed in Table 1 are reasonable limits on the values measured. The uncertainties reported in Table 1 are those developed from our formal testing of residuals, and should be regarded as 2-sigma uncertainties. They do not account for uncertainties in the envelope correction; however, as noted in the following paragraph, the practical effect of such uncertainties is not significant to our main conclusions.

Because limbs are envelopes over the high topography, we have applied corrections to account for hidden depressions (crater interiors) so that the axes and mean radii are appropri-
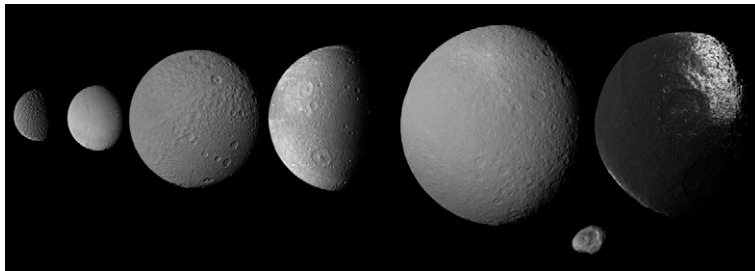

Fig. 1. Ellipsoidal icy satellites with Hyperion as an example of an irregularly shaped satellite. From left: Mimas, Enceladus, Tethys, Dione, Rhea, Hyperion, Iapetus.

Table 1
Satellite shapes

Satellite	a	b	c	Mean radius	a − c (km)	Im	Data
Mimas	207.4 ± 0.7	196.8 ± 0.6	190.6 ± 0.3	198.2 ± 0.5	16.8 ± 0.6	18	11,187
Enceladus	256.6 ± 0.6	251.4 ± 0.2	248.3 ± 0.2	252.1 ± 0.2	8.3 ± 0.6	26	19,027
Tethys	540.4 ± 0.8	531.1 ± 2.6	527.5 ± 2.0	533.0 ± 1.4	12.9 ± 1.9	7	3003
Dione	563.8 ± 0.9	561.0 ± 1.3	560.3 ± 1.3	561.7 ± 0.9	3.5 ± 1.2	14	8184
Rhea	767.2 ± 2.2	762.5 ± 0.8	763.1 ± 1.1	764.3 ± 2.2	4.1 ± 2.1	22	17,402
Iapetus	747.4 ± 3.1		712.4 ± 2.0	735.6 ± 3.0	35.0 ± 3.7	39	10,316

Note. Here we use a, b, c (all in km) to denote the Saturn-facing, orbit-facing, and polar radii. Im: number of images used; Data: number of data points.

ate for mean density calculations. Dermott and Thomas (1988) made the first estimation of this correction for Mimas. We have re-estimated the correction for Mimas (0.7 km), and for the other satellites: Enceladus, 0.15 km; Tethys 0.4 km; Dione 0.3 km; Rhea, 0.3 km; Iapetus 0.4 km. These values are uncertain, but overall estimates should be good to much less than 1 km. A 1-km error for the mean radius of Mimas, for example, would cause a 1.5% change in the mean density. Such a small change in mean density cannot be usefully interpreted geophysically because the constitutive materials and their porosities are uncertain. Effects of uncertainties in this correction on shape parameters ($a - c$, F) arise only as this parameter varies around the object; these variations are likely smaller than our measurement errors.

2.3. Interior models and supported topography

To evaluate how much shapes depart from matching equipotential surfaces, we use numerical 3-D models of the satellites' interiors based upon the techniques described in Thomas (1993). These models use 256,320 interior point masses within the specified ellipsoidal shape to simulate homogeneous or 2-layer bodies, and they account for tidal and rotational accelerations. The models give the potential at the surface accurate to an equivalent height of 25 m for 200-km radius bodies, or 1 part in 8000, and the models are sufficiently accurate to show the limitations of first-order linear approximations, such as the slight changes in equilibrium shapes for rapid rotators like Enceladus and Mimas (Dermott and Thomas, 1988, 1994). The change in the potential over the surface is expressed as a dynamic height (Vanicek and Krakiwsky, 1986; Thomas, 1993) by dividing the relative potential by an average gravitational acceleration. This quantity indicates how much relief is supported relative to an equipotential surface, and avoids ambiguities of simply reporting topographic deviations from some shape parameter. For most two-layer models we assume that the core has the same shape (i.e., axial ratios) as the surface. We have also calculated supported topography if the cores are relaxed (shapes in hydrostatic equilibrium) shapes, which would be more spherical than the surface given the higher density of the cores.

Equilibrium shapes are those where the physical surface is everywhere at the same potential, determined by the interior mass distribution and the rotational rate. For satellites in equilibrium, the shape is usually described well by an equilibrium shape factor, $F = (b - c)/(a - c) = 0.25$ (Chandrasekhar, 1969; Dermott, 1979), where the object rotates about the c axis, the a axis points to the primary, and the b axis is along the orbital motion. For rapidly rotating satellites, this parameter will decrease slightly (Dermott and Thomas, 1988). The value ($a - c$) is inversely proportional to the mean density, and decreases with central mass concentration. "Equilibrium" has also been used to denote ellipsoidal forms where a non-zero angle of friction might allow topography relative to an equipotential to be maintained (Holsapple, 2004; Sharma et al., 2006) in a rubble-pile constitution. We use equilibrium form to indicate approach to an equipotential surface as the objects we consider are not rub-

ble piles and it is also not clear that realistic rubble objects would maintain the low, uniform friction angles necessary to give good ellipsoidal forms, especially in the face of impact cratering.

Below we use two parameters to show deviations from equilibrium shapes: supported topography and $\Delta(b - c)$. The supported topography, T_s, is the total range (maximum–minimum) of dynamic heights over the object for the particular shape and interior model used. Uncertainties in T_s are reported based on maximum and minimum allowed values of the parameter F, or of ($a - c$), whichever is greater. $\Delta(b - c)$ is the difference in measured and theoretical ($b - c$) for the measured ($a - c$), calculated as the ($F_{obs} - F_{pred}$) × ($a - c$), where F_{obs} is the observed F, and F_{pred} is F predicted for a homogeneous object. Note that T_s is calculated for the model ellipsoid and does not reflect short wavelength variations in the actual limb profiles.

In our interior models we simply assume an icy outer shell of density 930 kg m^{-3}, appropriate for water ice with no porosity. Two problems might exist for this assumption: porosity that lowers the density, and other components that would raise it. Because the overall density for Tethys is only 970 kg m^{-3}, it would seem unlikely that common icy materials in the Saturn system much exceed this density. Such a small increase in the mantle density leads to very minor changes in T_s (39 m for Enceladus).

We use the residuals to the limb fits to characterize the roughness of the objects. These roughnesses are the root-mean square (rms) of the radial residual of each limb point from the best-fit ellipsoid. They may be given as kilometers or as fractions of the body's mean radius.

3. Shapes

3.1. Overview

Dimensions of six of the saturnian satellites are given in Tables 1 and 2. Table 3 lists supported topography from interior models and the range of surface gravities. Uncertainty in the mean density is a root-sum square of the fractional mass and volume uncertainties. For comparison, we include values of ($a - c$) if the object were homogeneous, ($a - c$)$_h$, with the specified mean density. Ground tracks of the limbs are shown in Fig. 2. Limb roughnesses for six satellites are shown in Fig. 3, in terms of km and as fractions of the mean radius.

The distribution of mean densities, 973 to 1608 kg m^{-3}, does not follow a simple radial or size-dependent pattern, as has been known, albeit less precisely, for some time (Campbell and Anderson, 1989; Dermott and Thomas, 1994). To first order, the shapes of Enceladus, Tethys, Dione, and Rhea are consistent with homogeneous, relaxed objects. Such a conclusion for Enceladus, at least, is surprising, and is discussed further below. Mimas is slightly more consistent with a model with a central mass concentration. Iapetus has the most spectacularly out-of-equilibrium shape, more than a 30-km difference from that predicted. Solutions differ in varying degrees from those obtained from Voyager limb data. Differ-

Table 2
Satellite shape parameters

Satellite	Mean radius (km)	$\rho\,(\mathrm{kg\,m^{-3}})$	$a-c$ (km)	$(a-c)_\mathrm{h}$ (km)	F_obs	F_pred	$\Delta(b-c)$ (km)
Mimas	198.2 ± 0.5	1150 ± 9	16.8 ± 0.6	19.7	0.37 ± 0.03	0.21	2.7
Enceladus	252.1 ± 0.2	1608 ± 5	8.3 ± 0.6	8.0	0.37 ± 0.04	0.23	1.1
Tethys	533.0 ± 1.4	973 ± 8	12.9 ± 1.9	14.7	0.28 ± 0.20	0.24	0.5
Dione	561.7 ± 0.9	1476 ± 7	3.5 ± 1.2	4.9	0.20 ± 0.37	0.25	0.2
Rhea	764.3 ± 2.2	1233 ± 11	4.1 ± 2.1	2.9	-0.15 ± 0.35	0.25	1.6
Iapetus	735.6 ± 3.0	1083 ± 13	35.0 ± 3.7	0.01	n/a	0.25	n/a

Note. ρ, mean density, determined from masses reported in Jacobson et al. (2006). $(a-c)_\mathrm{h}$ is predicted $(a-c)$ for homogeneous model. $\Delta(b-c)$ is $(F_\mathrm{obs} - F_\mathrm{pred}) \times (a-c)$.
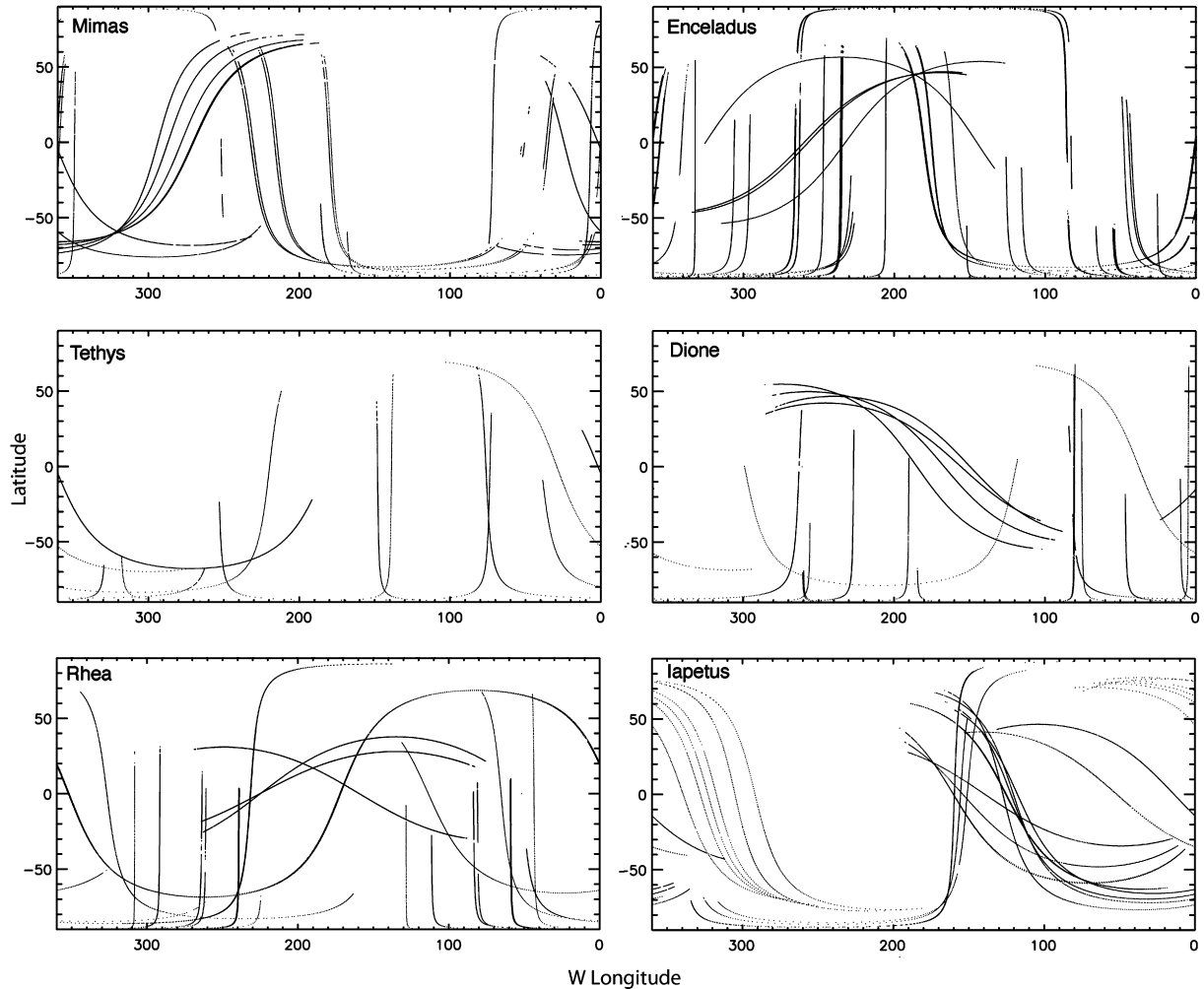

Fig. 2. Predicted limb data locations. Points show the predicted positions (latitude vs longitude, as measured west of the sub-Saturn longitude; positive latitudes are north) of the limb data on the reference ellipsoids. Gaps exist where images were noisy, especially in sections where Saturnshine illuminated the limb.

ences from the Voyager results in the $(a-c)$ parameter are 0.9 km for Mimas, 3.4 km for Enceladus, and 3.1 km for Tethys (Dermott and Thomas, 1988, 1994; Thomas and Dermott, 1991). The Voyager analyses, apart from using fewer and lower resolution data, apparently had more problems with geometric distortion from the vidicon than was realized. Those distortions are not an issue with the Cassini ISS CCD-based system, and our geometric calibration is in agreement with independent calibration performed by Owen (2003).

Table 3
Supported topography and gravity

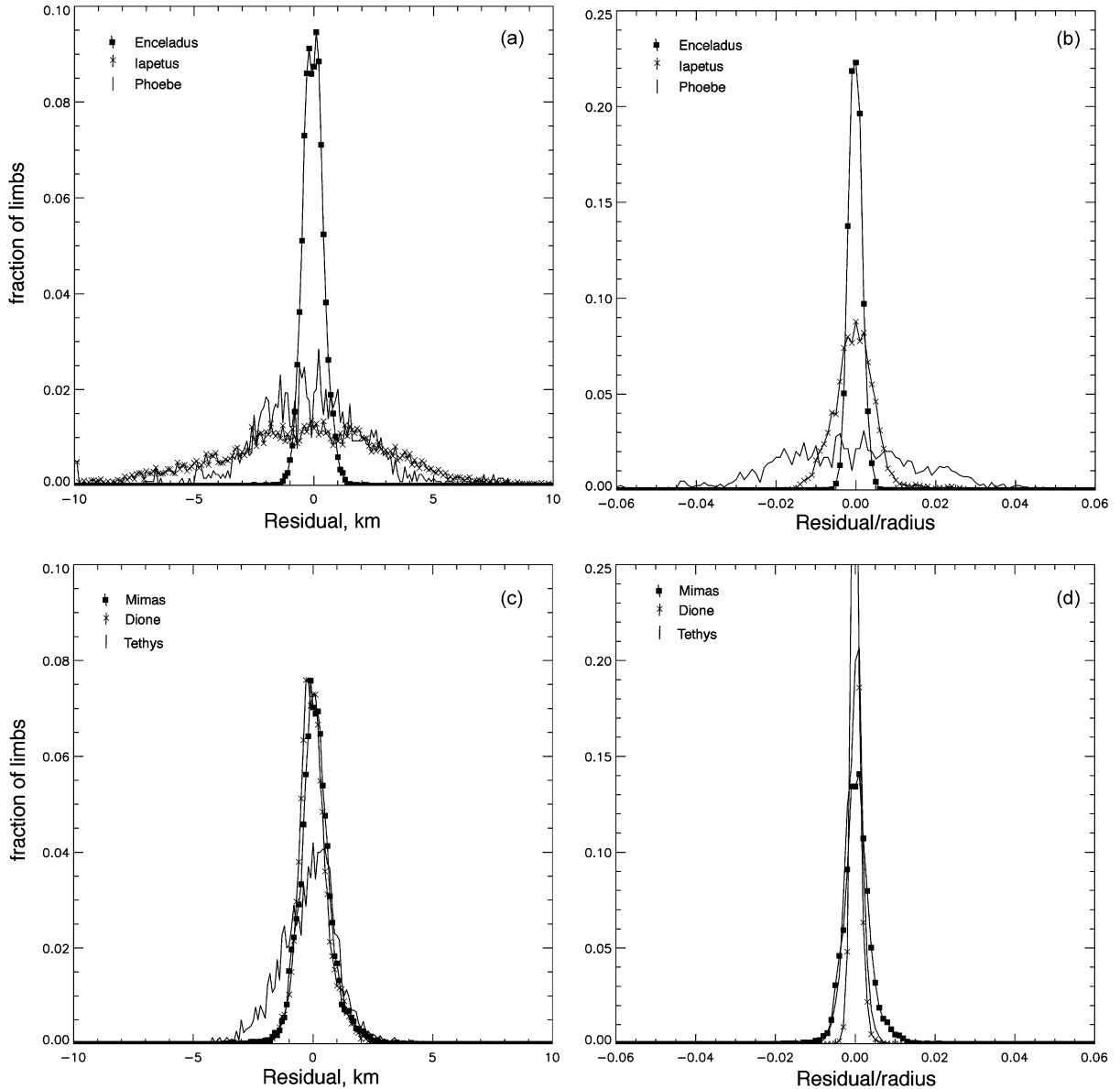| Satellite	T_sh	T_sd	$\mathrm{g\,cm\,s^{-2}}$
Mimas	1.87	1.49	5.9–6.5
Enceladus	0.51	1.20	11.1–11.4
Tethys	0.77	0.55	14.2–14.6
Dione	0.54	0.11	23.0–23.2
Rhea	1.02	0.94	26.2–26.4
Iapetus	14.3	15.9	22.2–22.4

Fig. 3. Limb roughness on saturnian satellites. Panels (a) and (c) display fractions of the limb data (number fractions) with residuals measured in km. Panels (b) and (d) show these results for the residuals divided by the satellite's mean radius. Note different scales due to different binning of the two types of residual measurements.

3.2. Mimas

Mimas is more spherical than it would be if it were a relaxed homogeneous object. However, its shape deviates from an ideal equilibrium form. An equilibrium shape of density 1150 kg m^{-3} at Mimas' orbital distance from Saturn would have an $(a-c)_h$ of 19.7 km, and an F of 0.21. The $\Delta(b-c)$ for Mimas is 2.7 km. Mimas, if homogeneous, supports 1.87 ± 0.26 km of relief (T_s) (Table 3). Because of the non-equilibrium shape, models of the interior with central mass concentrations can reduce the T_s only to ~1.5 km (mantle density of 930 kg m^{-3}, and core of density 3500 kg m^{-3}). The limbs' ground tracks (Fig. 2) do not cover the large crater Herschel (135 km diameter, 0° N 110° W); this incomplete coverage contributes to the shape uncertainty. The available information suggests

Mimas's relaxation is incomplete or has been masked at the 1–1.5 km level by density inhomogeneities.

We have compared control-point and limb solutions to evaluate further at what level the shape and the supported topography are significant. The control-point stereogrammetric solution is based upon 127 points, from 749 measurements in 67 images. This solution is not closed at low latitudes because coverage of the sub-Saturn region is limited by Mimas' orbit being inside that of Cassini. The control points show an ellipsoid within a km of the limb-derived one. The lack of closure of the control-point net may allow some "flexure" in the solution, but it suggests the limb solution is robust to accuracies substantially better than the $\Delta(b-c)$ of 2.7 km.

Does this shape have any relation to viscous relaxation? The rms residuals to the ellipsoid fit are 0.74 km, or ~0.4% of the mean radius. We conclude that the object is an ellipsoid, some-

thing formed by global processes, and not by impacts (localized changes). The limb residuals indicate that Mimas is securely in the group of ellipsoidal objects fundamentally different from Phoebe, and far smoother than Iapetus (Fig. 3).

Relaxation, however, does not mean that an object has completely reached a state where the physical surface matches an equipotential surface. Viscous relaxation takes time (Johnson and McGetchin, 1973; Thomas and Squyres, 1988) and is an asymptotic process. There is the possibility that even with favorable starting conditions, relaxation may not be "completed" before the thermal regime changes (Castillo et al., 2005, 2006). Equilibrium shapes in objects unlikely to creep might be achieved by sedimentary processes, but their apparent lack among most asteroids (Hestroffer, 2004; Holsapple, 2004; Richardson et al., 2005; Sharma et al., 2006) indicates viscous relaxation is the route to equilibrium shapes.

3.3. Enceladus

A differentiated structure has been prominent among ideas for Enceladus' interior since initial observation of its complex geology (Stevenson, 1982; Ellsworth and Schubert, 1983; Consolmagno, 1985; Ross and Schubert, 1989; Dermott and Thomas, 1994; Kargel and Pozio, 1996). Observation of ongoing activity (Porco et al., 2006; Spencer et al., 2006; Waite et al., 2006; Dougherty et al., 2006; Hansen et al., 2006) and the presence of a water-ice surface covering an object of mean density 1608 kg m^{-3} reinforce the likelihood of differentiation. However, Porco et al. (2006) note that Enceladus' shape is most consistent with a homogeneous interior; most notably its $(a-c)$ of 8.3 ± 0.6 km is indistinguishable from the homogeneous case of 8.0 km. In this work we have added further measurements of limbs and expanded the interior modeling.

We have determined the T_s for differentiated models of Enceladus with cores ranging in mean density from 1800 to 3000 kg m^{-3}, for varying shapes of the core, and for slightly different distances from Saturn. The results are given in Fig. 4. A homogeneous model requires a T_s of about 0.5 km, largely because the b-axis length makes F greater than the equilibrium value (0.38 vs 0.23). The differentiated models must support more topography the higher the core density. The examples with error bars (Fig. 4) have ellipsoidal cores with axes of the same relative proportions as the surface shapes. To test the magnitude of effects of modest changes in core shape, we allow for a 1 km elongation of the core a-axis, and decrease the core c-axis by 1 km. This change in core shape substantially decreases T_s (triangles in Fig. 4). An additional concern is whether Enceladus' orbit evolved after relaxation (Dermott and Thomas, 1994). Such motion is probably restricted to a narrow zone from 0.976 times the present distance to preclude having to pass through resonances from which it probably would not escape. The lower solid line plotted in Fig. 4 shows the effect on T_s by the nominal-shaped core models if relaxed at a distance of 0.976 times the present one.

Before evaluating the significance of these model results, one of their assumptions must be considered: lateral homogeneity. These models are strictly onion-layer, and assume a uniform
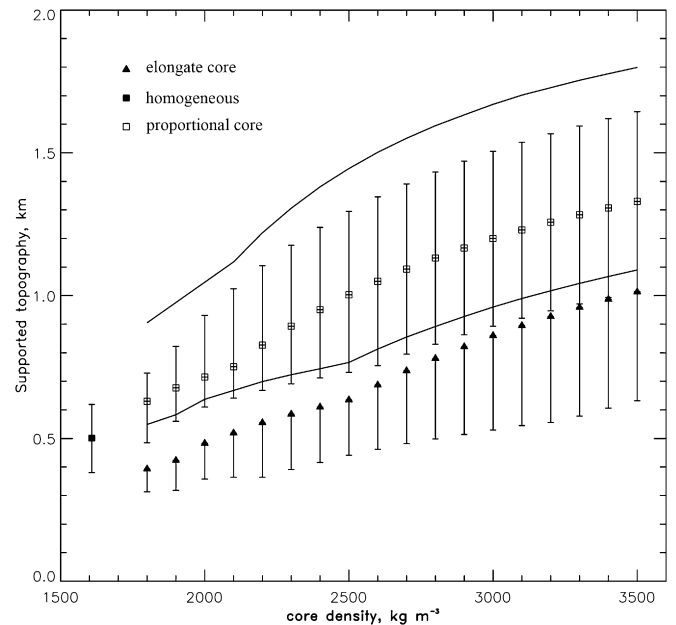

Fig. 4. Supported topography, T_s, on Enceladus for different interior models. Homogeneous model is at left; its error bars are dominated by the non-equilibrium value of $(b-c)/(a-c)$. Open squares show models with cores of specified density under ice shells of density 930 kg m^{-3}. Error bars are calculated from the permissible range of $(a-c)$ and of the shape parameter F. The cores have the same axial proportions as the surface. Triangles with only lower error bars are results for cores with 1 km longer a axes, and 1 km reduced c axes. The lower solid line shows results for the nominal core shape if equilibrated at 0.976 times the current distance from Saturn. The upper solid line shows results at the current distance if the core has an equilibrium shape appropriate for its density.

density throughout a core or mantle. However, the observed geology of Enceladus has notable lateral variation. The surface shows a huge range of apparent ages (Boyce and Plescia, 1984; Plescia and Boyce, 1985; Porco et al., 2006), and different stages of crater relaxation. The range of crater morphologies suggests different levels of heat flow in different surface regions, which would require significant variations in ice shell porosity and/or composition. The current activity isolated near the south pole, and the distinct polar geologic province (Porco et al., 2006; Helfenstein et al., 2006) also point toward lateral heterogeneity at least a few km in depth. The supported topography of the differentiated model can be reduced by including circum-polar zones of reduced density. For example, a 15% reduction in density of the outer 25 km, from the poles to 56° latitude reduces T_s by over 200 m. However, putting only one zone of reduced (or increased) density at the south pole increases the supported topography. More complicated arrangements of density would be needed to reduce the T_s further, but this example illustrates the scale of effects that may be involved.

Does the observed geology and topography indicate particular features that might explain the difference of the ellipsoidal fit from the geoid, and at what level is the actual ellipsoidal fit significant? Profiles of the residuals to the fit ellipsoid show the scale of some of the geological diversity that might be reflected at depth. Latitudinally averaged limb residuals for Enceladus are shown in Fig. 5. The maximum range of global-fit residu-
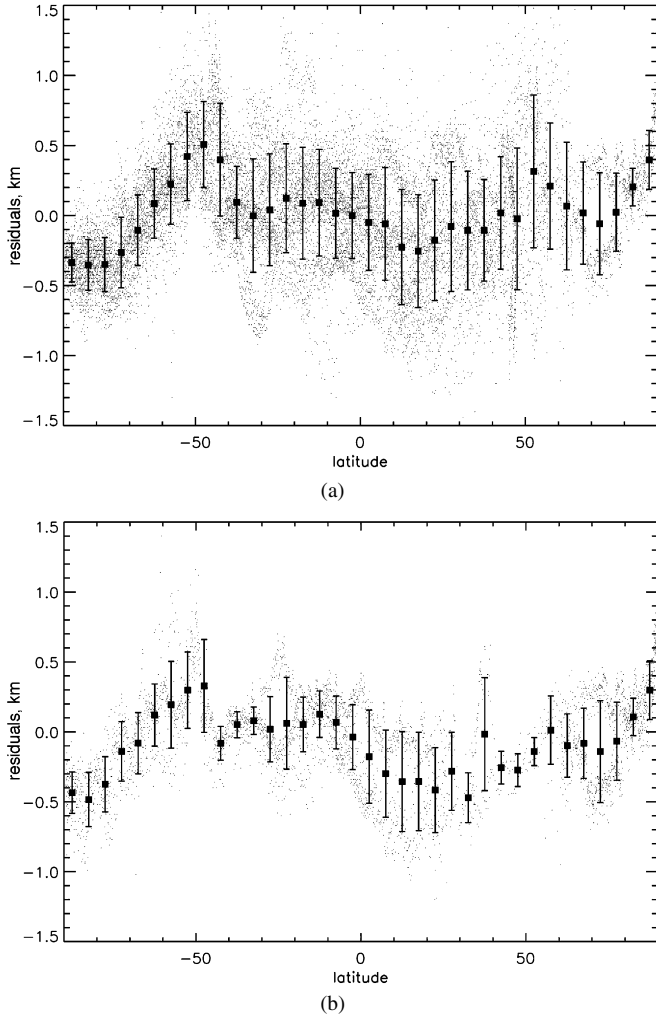
(a)

(b)

Fig. 5. Latitudinally averaged limb-fit residuals for Enceladus. (a) All Enceladus data shown by small dots; large symbols are 5° averages, error bars are standard deviations. (b) Data from four transit images that show both poles. These data fall close to the 90–270 longitudes.
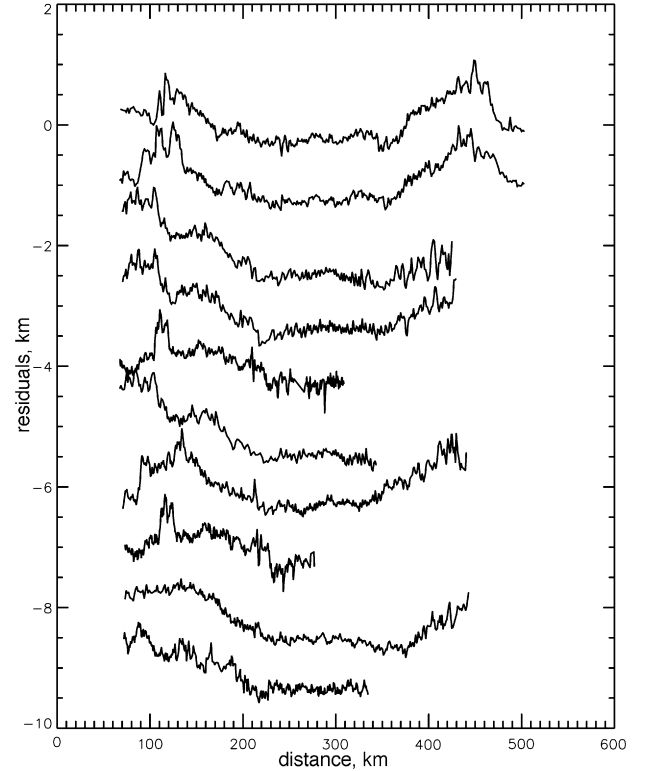

Fig. 6. Individual profiles of limb-fit residuals across the south pole of Enceladus. Left-hand point is at 40° S. All profiles cross within 1.5° of the pole. Vertical exaggeration = 65×.

als reach nearly 2.5 km. The latitudinally averaged values have a range of nearly 900 m. The significance of an ellipsoidal fit (not the range of allowable shapes) may be estimated by the variation of the latitudinally averaged values, which have a standard deviation of 0.21 km, or an effective full range of 0.4 km. Changes of axes (hemispherical wavelength changes) introduce roughly half as much change of T_s. Thus, we conclude that it is probably not productive to consider supported topography less than 0.2 km on Enceladus.

Of particular interest in the residual profiles is the south polar region which may be described as a rimmed depression (Fig. 6). The "tiger stripes," fractures with associated albedo features and the sites of observed plumes (Porco et al., 2006), occupy a region from the pole to about 65° S, or the portions of the profiles below the reference ellipsoid. Compressional tectonic features in the region 50°–65° S approximately coincide with the elevated portions of the profiles in Fig. 6, and considered with extentional features reaching to the equatorial region are consistent with a global, or at least hemispherical, change in figure of Enceladus where the polar dimension is shortened

(Helfenstein et al., 2006). However, the extentional tiger stripe features suggest a later tectonic phase distinct from any global figure change. Conversely, any change in figure is not simply a result of depression at the pole.

The venting may indicate melting at depth (Porco et al., 2006), which would locally increase the density, especially if it also eliminated pore space. The venting might over time remove mass and enhance the depressed part of the feature. The volume of the depression, $\sim 1.3 \times 10^4$ km^3, if taken to be the deficit from the reference ellipsoid, would require $\sim 3 \times 10^6$ years to form if produced by the present venting flux of ~ 150 kg/s of water vapor (Hansen et al., 2006). The particulate flux is comparable (Porco et al., 2006), thus timescales might be less. However, because the south polar province includes at least as much topography above the reference ellipsoid as below, there is no way to define reliably a "depression" volume.

Nimmo and Pappalardo (2006) proposed that the active region is located at the south pole of Enceladus due to diapir-induced reorientation. Because the $(a - c)$ of Enceladus is appropriate for a relaxed homogeneous object, and is too large for a differentiated one (c axis too small), if reorientation occurred, a decrease in density at depth, with little surface deformation, would be required. Forming a zone of lower density would either require some phase change, or some compensating physical motion (solid state deformation) to occur. Modeling such deformations is beyond the scope of this work

Returning to Fig. 4, even considering the 200 m significance level, the simple differentiated models do not describe the shape

of Enceladus. Those with irregularly-shaped cores, and perhaps some variation in ice shell densities might be consistent with the shape if the core mean density is less than ~2200 kg m^{-3}. While equilibration closer to Saturn might explain the shape better, it would still need to support this topography in current conditions. The tectonic patterns suggest polar flattening of an indeterminate amount. If Enceladus were differentiated and relaxed, and then flattened to the present form, it would require effects at depth of nearly hemispherical extent; the amplitude of topography of the south polar tectonic province is only a small fraction of the differences between homogeneous and highly differentiated shapes.

In sum, the shape of Enceladus suggests that if it is differentiated it has a large, low-density core, the core itself might have inhomogeneities in density or shape, and an outer ice shell may be inhomogeneous in density by 10% or more on nearly hemispherical scales. Fully relaxed, radially differentiated, laterally homogeneous models do not explain the shape.

3.4. Tethys

Tethys' shape is consistent with that of a relaxed object in hydrostatic equilibrium, although the satellite's roughness (Giese et al., 2006) and the less-than-desirable image-coverage to date create large uncertainties in the results. The supported topography for a homogeneous model is 0.77, +0.74, −0.22 km. Tethys' shape is thus almost consistent with the interior being homogeneous. The equilibrium shape of any differentiated model differs little from the homogeneous case because the very low mean density requires that any core that is present must be very small. For our standard mantle and core densities of 930 and 3000 kg m^{-3}, Tethys has supported topography of 0.55, +0.79, −0.06 km. The core would constitute 0.06 of the satellite's mass and have a radius of 145 km.

3.5. Dione

Dione's shape is consistent with that of a relaxed object, and the $(a - c)$ is marginally consistent with the homogeneous case. The homogeneous model supports 0.54, +0.49, −0.44 km of topography. Our standard core model would support 0.11 km, +0.6 km, and is thus our best differentiated model. (For the standard core model, all shape uncertainties increase the supported topography from the nominal value, thus the single error value.) This model has a core mass ratio of 0.54, and a core radius of 360 km.

3.6. Rhea

Rhea's $(a - c)$ is consistent with the satellite being in hydrostatic equilibrium, but the placement of limb profiles results in significant uncertainties in the a axis and in the relative values of the b and c axes; the nominal solution has $c > b$, which would imply lateral inhomogeneities. A homogeneous Rhea would support 1.02, +1.74, −0.16 km of topography. Our standard mantle/core combination has a core mass ratio of 0.36, and supports 0.94, +1.12, −0.71 km of topography.

While the measurements may permit a shape consistent with a relaxed, differentiated structure, the uncertainties also allow for substantially different interior models. For these examples, the uncertainty in $(a - c)$ drives the highest supported topography.

3.7. Iapetus

For decades—even centuries, the major Iapetus puzzle was how the satellite's leading and trailing sides acquired albedos that differed by a factor of ~10. Four years before Cassini's arrival, Denk et al. (2000), using Voyager images, found a new conundrum: Iapetus has a decidedly non-spherical shape, something not expected given the apparently relaxed nature of objects that are considerably smaller than this large outer moon. Images obtained in the first year of Cassini's orbital tour have documented this non-spherical shape and have revealed significant global tectonism on Iapetus.

Iapetus is markedly non-spherical; the best-fit triaxial shape is 748.8, 743.2, 712.4 km, with the long axis at 320° W longitude. An oblate spheroid of axes 747.4 by 712.4 km is within the allowed residuals. We treat Iapetus as an oblate spheroid (Table 1). The gap in limbs in the 200°–280° W longitude range, and the low resolution of most images between 280° and 360° W raises some concern about the fit's accuracy, but subdivisions of the data yield shapes within a few km of our adopted values, and errors would have to be 20 km or more to qualitatively alter the conclusions. The satellite's density and spin rate predict an axial difference of only ~10 m, not the measured difference of 35 km. Because of the absolute value of Iapetus' limbs roughness (Fig. 3a), we might suspect that Iapetus has never relaxed. However, the relative roughness, less than 1% of the mean radius, Fig. 3b (also see Fig. 1), indicates that Iapetus' shape indeed is an oblate spheroid, probably a result of relaxation, or approach to relaxation. Such relaxation and subsequent freezing of the shape would have to have occurred at a higher spin rate.

Iapetus has topography that dwarfs that on Enceladus (Fig. 7). Two key departures from the reference spheroid on Iapetus are the equatorial ridge (Porco et al., 2005; Denk et al., 2005) and large craters (Fig. 7). The equatorial ridge is crossed by limb profiles at different locations and at different angles (see Fig. 2). Removing the equatorial ridge portions from the data reduces the equatorial fit axes by 1.2 km.

Iapetus currently rotates synchronously with its orbital period of 79 days. Because of the satellite's distance from Saturn, despinning in the age of the Solar System has posed some theoretical challenges, requiring a very dissipative interior, with a dissipation factor, Q, <50 (Peale, 1977). Today's measured shape adds an interesting aspect to this puzzle since the oblate form is consistent with relaxation at a spin period of 16.4 + 0.9, −0.8 h for a homogeneous body. (If Iapetus were differentiated with our standard mantle/core densities, the shape would be consistent with a spin period of 15.2 + 0.8, −0.7 h.) Furthermore, according to this model, the satellite must have achieved rigidity while at that spin period and have deformed little subsequently. Iapetus, if homogeneous, currently supports 14.3 km of topography; our standard mantle/core model would
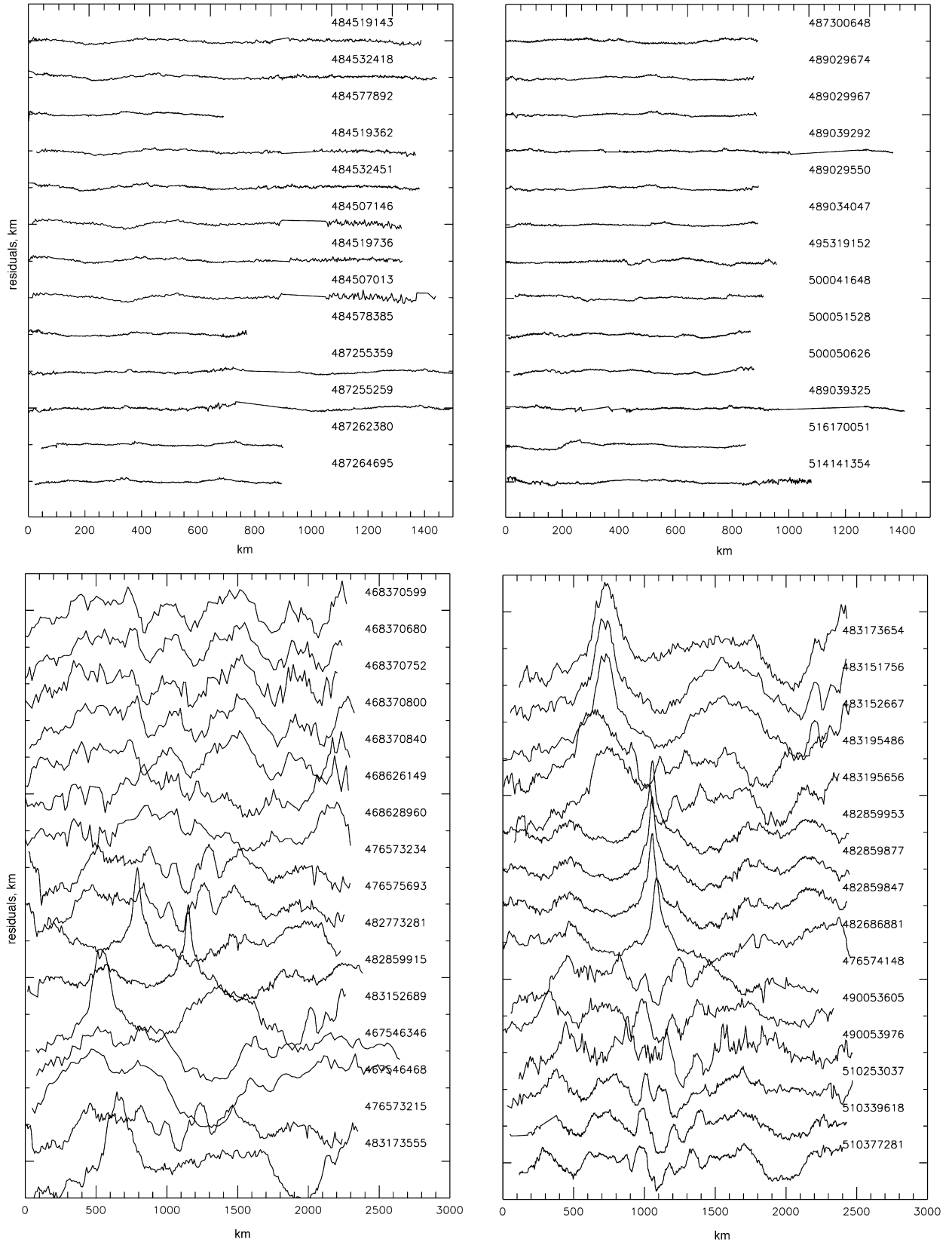
Fig. 7. Limb topography on Enceladus (top panels) and Iapetus (bottom panels) at the same vertical scales. Four low-resolution limbs for Iapetus are not included. Each profile is labeled with the corresponding image number. Vertical exaggeration is a factor of 26 for Enceladus, 53 for Iapetus.

instead support 15.9 km of topography. These findings place serious constraints upon any thermal history (Castillo et al., 2005, 2006), which may involve very early heating promoted by CAI's (calcium–aluminum-rich inclusions), chiefly ^{26}Al. Re-

gardless of the details of the thermal history, Iapetus is unique in the relative size of a fossil rotational bulge.

4. Systematics of the Saturn satellite shapes and topography

As a group, do the saturnian satellites suggest common processes of relaxation, a certain level of non-hydrostatic topography, systematic modifications to relaxed objects, or no real pattern of shapes? Figs. 8–10 present three systematic views of the shapes as represented by limb roughness, departures from equilibrium shapes, and supported topography.

The limb roughness describes how well the objects are represented by ellipsoids. Except for Phoebe, the satellites are fit by ellipsoids to well less than 1% of their mean radii. There is a factor of nearly 4 in relative limb roughness between Phoebe and Iapetus, but there is also a factor of 4 between Dione and Iapetus. Other small satellites and asteroids have roughnesses of 2.5–8% (Thomas, 1989). The dominant shaping mechanism for satellites in Fig. 8, except Phoebe, is something other than impacts.

The ellipsoids are compared to equilibrium shapes in Fig. 9. Randomly shaped ellipsoids with $a > b > c$, would be expected to have a range of F from 0 to 1. The values are clustered (Fig. 9a) at values close to the theoretical equilibrium ones, and are not well scattered between 0 and 1. The values of $(a - c)$ and

those predicted for homogeneous models are shown in Fig. 9b. Iapetus stands out as the only one far from the prediction. Differentiated models would move the predicted values of $(a - c)$ in Fig. 9b slightly to the left. As noted above, while differentiated structure would improve the match of predicted with observed $(a - c)$ for Mimas, it would not significantly reduce the supported topography because of the $\Delta(b - c)$.

Finally, the T_s for homogeneous models is shown in Fig. 10. Iapetus here stands as unique, far more so than for its roughness factor, which is the reason we may assign a fossil shape
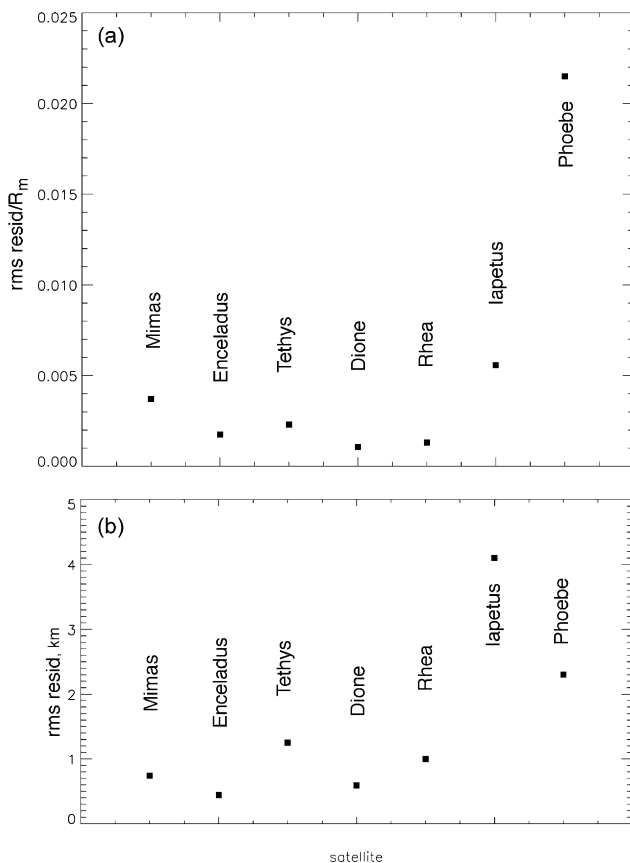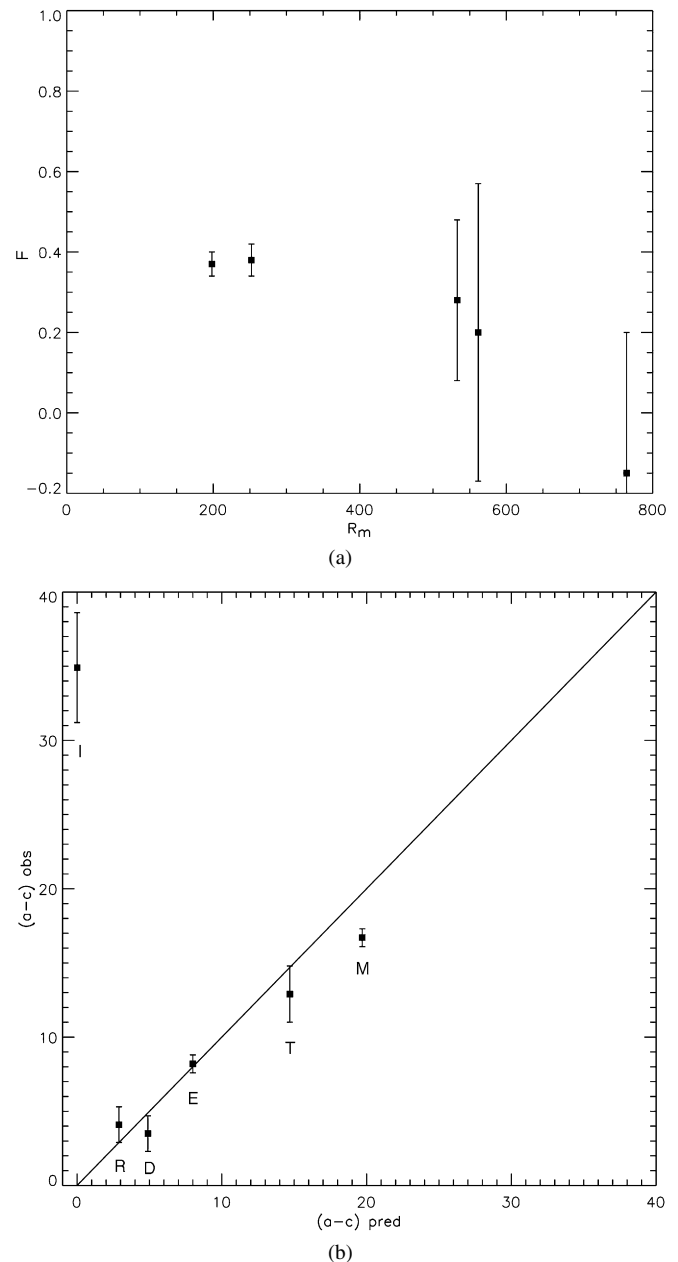

(a)

Fig. 8. Roughness of limbs of saturnian satellites. Plotted quantities are the root mean square residuals to the limb fits (a) as a fraction of the object's mean radius and (b) as absolute amounts.

(b)

Fig. 9. (a) Approach to equilibrium shapes. The observed factor F $((b - c)/(a - c))$ plotted against object mean radius. Equilibrium values for F are 0.21 for Mimas, 0.23 for Enceladus, 0.24 for Tethys, and 0.25 for Dione, and Rhea. Iapetus is not included in this plot. (b) Observed and predicted differences in long and short axes of saturnian satellites. The predicted values assume that the object is homogeneous.
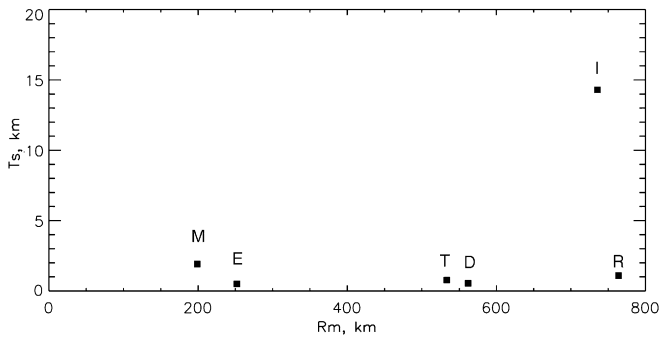
Fig. 10. Supported topography for the six icy satellites versus mean radius.

to Iapetus. These three measures taken together strongly suggest that Mimas, Enceladus, Tethys, Dione, and Rhea have at one time approached a relaxed form, retaining less than 2 km of globally supported topography. Iapetus' relative roughness and non-triaxial form strongly suggest early relaxation at high spin rate. Only Iapetus has a significant fossil form. Any fossil forms on the other satellites are currently largely obscured by uncertainties in the global shapes and interior configurations.

Iapetus has apparently preserved its shape from an early, rapid spin. Spin changes for the other satellites, as triaxial ellipsoids, probably would arise from orbital evolution, and as mentioned earlier (see also Dermott and Thomas, 1994) are probably of limited extent. Changes in shape due to differentiation are an additional possibility. Given the uncertainties in some of the shapes, we look here only at Enceladus. At its current orbit, a differentiated (core of density 3000 kg m^{-3}, mantle of 930 kg m^{-3}, equilibrium-shaped Enceladus would have an $(a - c)$ of 6.0 km, 2 km less than the homogeneous case. Of course, the present non-equilibrium shape is a concern, although the disequilibrium implied by Enceladus' value of F is much smaller than that implied by the difference in $(a - c)$. Ignoring possible volume changes, going from a homogeneous structure to a differentiated one would decrease the a axis by 1.2 km, increase the b axis by 0.36 km, and increase the c axis by 0.8 km. The tectonic patterns on Enceladus if anything suggest the opposite change in shape (Helfenstein et al., 2006), but because the tectonic forms largely apply to the southern hemisphere, and there is no firm information on the amount of strain involved, we can only say the pattern of tectonics would have to post date any global shape changes caused by differentiation.

Iapetus has apparently retained its shape from very early on, and thus should have an excellent record of the cumulative topographic effects of cratering on old surfaces in the Saturn system. Because the cratering rate for extra-Saturn material increases toward Saturn, Mimas should have experienced a much higher cratering flux (Lissauer et al., 1988). Mimas has a smoother limb than Iapetus, which because Mimas' surface is almost certainly not subject to significant internally driven modification, leads to the conclusion that its approximate relaxation occurred after Iapetus' shape was frozen. Such would also be true for the other icy satellites that display limbs much smoother than Iapetus. Certainly for Enceladus and Dione the obvious tectonic effects signify much younger surfaces than that of Iapetus.

5. Summary

All six icy saturnian satellites appear to have approached relaxed, equilibrium shapes at some point in their evolution, but all support at least several hundred meters of global topography. Enceladus' geology suggests that it is differentiated; lateral variation in the density of an icy mantle would be required to bring its surface close to the globally relaxed form it appears to have. Such inhomogeneity is consistent with other lines of evidence for Enceladus' interior structure. Iapetus supports a fossil bulge of over 30 km, and provides a benchmark for post global relaxation modification of the shape by impact cratering.

References

Boyce, J.M., Plescia, J.B., 1984. Chronology of surface units on the icy satellites of Saturn. In: Ices in the Solar System. Proceedings of the Advanced Research Workshop, Nice, France, January 16–19, 1984 (A86-23051 09-91). D. Reidel Publishing, Dordrecht, pp. 791–804.

Campbell, J.K., Anderson, J.D., 1989. Gravity field of the saturnian system from Pioneer and Voyager tracking data. Astron. J. 97, 1485–1495.

Castillo, J.C., Matson, D.L., Sotin, C., Johnson, T.V., Lunine, J.I., Thomas, P.C., 2005. A geophysical study of Iapetus: The need for and consequences of ^{26}Al. Bull. Am. Astron. Soc. 37, 705.

Castillo, J.C., Matson, D.L., Sotin, C., Johnson, T.V., Lunine, J.I., Thomas, P.C., 2006. A new understanding of the internal evolution of saturnian icy satellites from Cassini observations. Lunar Planet. Sci. 37. Abstract 2200.

Chandrasekhar, S., 1969. Ellipsoidal Figures of Equilibrium. Yale Univ. Press, New Haven.

Consolmagno, G.J., 1985. Resurfacing Saturn's satellites—Models of partial differentiation and expansion. Icarus 64, 401–413.

Denk, T., Matz, K.-D., Roatsch, T., Wolf, U., Wagner, R.J., Neukum, G., Jaumann, R., 2000. Iapetus (1): Size, topography, surface structures, craters. Lunar Planet. Sci. 31. Abstract 1596.

Denk, T., and 13 colleagues, 2005. First imaging results from the Iapetus B/C Flyby of the Cassini Spacecraft. Lunar Planet. Sci. 36. Abstract 2268.

Dermott, S.F., 1979. Shapes and gravitational moments of satellites and asteroids. Icarus 37, 575–586.

Dermott, S.F., Thomas, P.C., 1988. The shape and internal structure of Mimas. Icarus 73, 25–65.

Dermott, S.F., Thomas, P.C., 1994. The determination of the mass and mean density of Enceladus from its observed shape. Icarus 109, 241–257.

Dougherty, M.K., Khurana, K.K., Neubauer, F.M., Russell, C.T., Saur, J., Leisner, J.S., Burton, M.E., 2006. Identification of a dynamic atmosphere at Enceladus with the Cassini magnetometer. Science 311, 1406–1409.

Ellsworth, K., Schubert, G., 1983. Saturn's icy satellites—Thermal and structural models. Icarus 54, 490–510.

Giese, B., Wagner, R., Neukum, G., Helfenstein, P., Porco, C.C., 2006. Topographic features of Ithaca Chasma, Tethys. Lunar Planet. Sci. 37. Abstract 1749.

Hansen, C.J., Esposito, L., Stewart, A.I.F., Colwell, J., Hendrix, A., Pryor, W., Shemansky, D., West, R., 2006. Enceladus' water vapor plume. Science 311, 1422–1425.

Holsapple, K.A., 2004. Equilibrium figures of spinning bodies with self-gravity. Icarus 172, 272–303.

Helfenstein, P., and 16 colleagues, 2006. Patterns of fracture and tectonic convergence near the South Pole of Enceladus. Lunar Planet. Sci. 37. Abstract 2182.

Hestroffer, D., 2004. On equilibrium shapes among binary asteroids. Bull. Am. Astron. Soc., DAA Meeting 35. Abstract 07.10.

Jacobson, R.A., Antreasian, P.G., Bordi, J.J., Criddle, K.E., Ionasescu, R., Jones, J.B., Mackenzie, R.A., Pelletier, F.J., Owen Jr., W.M., Roth, D.C., Stauch, J.R., 2006. The gravitational field of Saturn and the masses of its major satellites. Astron. J. 132, 2520–2526.

Johnson, T.V., McGetchin, T.R., 1973. Topography on satellite surfaces and the shape of asteroids. Icarus 18, 612–620.

Kargel, J.S., Pozio, S., 1996. The volcanic and tectonic history of Enceladus. Icarus 119, 385–404.

Lissauer, J.J., Squyres, S.W., Hartmann, W.K., 1988. Bombardment history of the Saturn system. J. Geophys. Res. 93, 13776–13804.

Nimmo, F., Pappalardo, R.T., 2006. Diapir-induced reorientation of Saturn's moon Enceladus. Nature 441, 614–616.

Owen Jr., W.M., 2003. Cassini ISS geometric calibration. In: JPL Interoffice Memorandum 312. E-2003-001.

Peale, S.J., 1977. Rotation histories of the natural satellites. In: Burns, J.A. (Ed.), Satellites. Univ. of Arizona Press, Tucson, AZ, pp. 87–112.

Plescia, J.B., Boyce, J.M., 1985. Impact cratering history of the saturnian satellites. J. Geophys. Res. 90, 2029–2037.

Porco, C.C., and 34 colleagues, 2005. Cassini imaging science: Initial results on Phoebe and Iapetus. Science 307, 1237–1242.

Porco, C.C., and 24 colleagues, 2006. Cassini observes the active South Pole of Enceladus. Science 311, 1393–1401.

Richardson, D.C., Elankumaran, C.P., Sanderson, R.E., 2005. Numerical experiments with rubble piles: Equilibrium shapes and spins. Icarus 173, 349–361.

Ross, M.N., Schubert, G., 1989. Viscoelastic models of tidal heating in Encedalus. Icarus 78, 90–101.

Sharma, I., Jenkins, J.T., Burns, J.A., 2006. Tidal encounters of ellipsoidal granular asteroids with planets. Icarus 183, 312–330.

Spencer, J.R., Pearl, J.C., Segura, M., Flasar, F.M., Mamoutkine, A., Romani, P., Buratti, B.J., Hendrix, A.R., Spilker, L.J., Lopes, R.M.C., 2006. Cassini encounters Enceladus: Background and the discovery of a south polar hot spot. Science 311, 1401–1405.

Stevenson, D.J., 1982. Volcanism and igneous processes in small icy satellites. Nature 298, 142–144.

Thomas, P., 1989. Shapes of small satellites. Icarus 77, 248–274.

Thomas, P.C., 1993. Gravity, tides, and topography on small satellites and asteroids—Application to surface features of the martian satellites. Icarus 105, 326–334.

Thomas, P.C., Dermott, S.F., 1991. The shape of Tethys. Icarus 94, 391–398.

Thomas, P.C., and 9 colleagues, 1998. The shape of Io from Galileo limb measurements. Icarus 135, 175–180.

Thomas, P.J., Squyres, S.W., 1988. Relaxation of impact basins on icy satellites. J. Geophys. Res. 93, 14919–14932.

Vanicek, P., Krakiwsky, E.J., 1986. Geodesy: The Concepts, second ed. Elsevier, New York.

Waite Jr., J.H., Combi, M.R., Ip, W., Cravens, T.E., McNutt Jr., R.L., Kasprzak, W., Yelle, R., Luhmann, J., Niemann, H., Gell, D., Magee, B., Fletcher, G., Lunine, J., Tseng, W., 2006. Cassini ion and neutral mass spectrometer: Enceladus plume composition and structure. Science 311, 1419–1422.